RESEARCH ARTICLE

Ahmed Mohmed DAFALLA, Fangming JIANG

Effect of catalyst layer mesoscopic pore-morphology on cold start process of PEM fuel cells

Abstract   Water transport is of paramount importance to the cold start of proton exchange membrane fuel cells (PEMFCs). Analysis of water transport in cathode catalyst layer (CCL) during cold start reveals the distinct characteristics from the normal temperature operation. This work studies the effect of CCL mesoscopic pore-morphology on PEMFC cold start. The CCL mesoscale morphology is characterized by two tortuosity factors of the ionomer network and pore structure, respectively. The simulation results demonstrate that the mesoscale morphology of CCL has a significant influence on the performance of PEMFC cold start. It was found that cold-starting of a cell with a CCL of less tortuous mesoscale morphology can succeed, whereas starting up a cell with a CCL of more tortuous mesoscale morphology may fail. The CCL of less tortuous pore structure reduces the water back diffusion resistance from the CCL to proton exchange membrane (PEM), thus enhancing the water storage in PEM, while reducing the tortuosity in ionomer network of CCL is found to enhance the water transport in and the water removal from CCL. For the sake of better cold start performance, novel preparation methods, which can create catalyst layers of larger size primary pores and less tortuous pore structure and ionomer network, are desirable.

Ahmed Mohmed DAFALLA
Laboratory of Advanced Energy Systems, Guangdong Key Laboratory of New and Renewable Energy Research and Development, CAS Key Laboratory of Renewable Energy, Guangzhou Institute of Energy Conversion, Chinese Academy of Sciences (CAS), Guangzhou 510640, China; University of Chinese Academy of Sciences, Beijing 100049, China

Fangming JIANG (✉)
Laboratory of Advanced Energy Systems, Guangdong Key Laboratory of New and Renewable Energy Research and Development, CAS Key Laboratory of Renewable Energy, Guangzhou Institute of Energy Conversion, Chinese Academy of Sciences (CAS), Guangzhou 510640, China
E-mail: fm_jiang2000@yahoo.com

1   Introduction

Proton exchange membrane fuel cell (PEMFC) is recognized as an attractive energy conversion device for future power generation sources, owing to its great advantages such as high efficiency, low-emissions, compact structure, and silence [1,2]. Nevertheless, many challenges/barriers face the commercialization of the PEMFC to be used as vehicle engine [3,4]. One of the barriers is its ability to achieve a successful quick startup from subfreezing environment [5]; the self-startup without any external auxiliary heating is the most desired. The accumulative ice in the cathode catalyst layer (CCL) is a primary factor that leads to the operational failure of the cell [6]. Understanding the water transport and ice formation mechanism in the cathode electrode is crucial for developing new techniques or designs toward enhancing the self- cold start performance [7,8].

Among the components of PEMFCs, the CCL is placed between the membrane and the gas diffusion layer (GDL), and it is where the electrochemical reaction (ECR) takes place. The structural morphology of the catalyst layer (CL) is manufactured to ensure the balance of proton and electron transport with reactants/product transport, thus the CL has the most complex structure [9]. Concurrently, in subfreezing operation, the existence of ice inside the CL aggravates the transport limitation by blocking the gas transport pathway and covering the active reaction area [10,11], consequently impacting the fate of cold startup or even resulting in the failure of cold start [12].

The complex transport phenomena involved within the CL is strongly affected by the mesoscale morphology of the CL [13]. Extensive research efforts have been made to develop and enhance the CCL of PEMFC. Experimentally, various CL morphologies were widely tested at different platinum loadings [14–16], and ionomer loadings [17].

Although the experimental investigations are very useful and valuable, it is too time-consuming, costly [18], and may not be able to give much insightful information concerning the multidisciplinary transport in CCL, which is strongly needed. For PEMFC particularly, there are a large number of variables that are involved in studying the transport phenomena [19]. Hence, numerical models are powerful tools to fundamentally elucidate the transport processes in CCL. Different numerical models that have been established to improve the overall cell performance and enhance the structure of its multicomponent, considering various global scales such as macro-scale model [20,21], mesoscopic model [22,23], agglomerate model [24,25], are comprehensively reviewed and reported [26].

In this regard, Sassin et al. [27] studied the effect of porosity and thickness of CL on PEMFC transport limitations. They found that decreasing the porosity of thicker CLs results in an increase in the mass transport resistance, but has no effect on electrical transport resistance. The impact of CL morphology on PEMFC performance and local distributions of key parameters was investigated by Carcadea et al. [28], and an optimum range of ionomer was determined. Besides, their investigation showed that the active electrochemical area could considerably increase the overall current density by using a mixed cathode catalyst. They stated as well that a higher platinum loading and lower particle radius were beneficial to achieve a better PEMFC performance. Molaeimanesh et al. [29] performed a Lattice Boltzmann simulation to capture the influence of CL morphology on PEMFC cathode, and both uniformly and stochastically presented the arrangements of the agglomerates. They also showed the species transport in the pore region and the charge distribution in the interface between the CL and membrane.

Most of the previous numerical models that described the effect of CL morphology on PEMFC were generally focused on the normal operating condition and rarely related to the cold start process. Nandy et al. [30] demonstrated the effect of CCL pore volume on cold start behavior under both isothermal and non-isothermal operating conditions. Luo et al. [31] stated that increasing the porosity and thickness of CL resulted in less ice formation. Hiramitsu et al. [32] indicated the importance of ionomer as a carrier of reactant gas, protons, and water. Besides, they found that using a CL that characterized by higher ionomer content was beneficial for both the cold start-up and durability. Xie et al. [33] found that under the normal operating condition, the ionomer carbon ratio (I/C) improved the humidity tolerance of the membrane, while under the subzero operating condition, the ionomer carbon ratio did not affect the water availability for different I/C ratio cases due to the ice formation. Additionally, more ice was formed for the cases of higher I/C ratios. Ko and Ju [34] employed a three-dimensional cold start model to examine the influence of different CL designs on cold start

performance. They reported that the ionomer fraction and weight ratio of platinum to carbon support of CL had a significant impact on the ice storage capacity and water uptake by the CL. Recently, He et al. [35] established a 2D lattice Boltzmann model to study the ice melting phenomena in porous media during the cold start of PEMFC. They examined the effect of key GDL parameters such as porosity, carbon fiber layer number and length on the ice melting behavior, and found that the ice melting rate in the GDL could be considerably increased by reducing the GDL porosity.

Despite the research that has been conducted, still there is a need to gain a better understanding of the water transport and accumulation mechanism in the CCL, in particular with the presence of ice in the active reaction area at sub-freezing temperatures. The purpose of this paper is to gain further insight into the water transport resistance in the CL considering the existence of ice with regard to the morphology of CL. First, theoretical analyses are provided to quantify the water transport capability by the pores and ionomer component in CL, and to quantify the water transport (back diffusion) resistance in the CL and membrane during cold start operation. Then, in light of the work by Wu and Jiang [36], the CL morphology is characterized by the tortuosity of individual component, and the effect of different CL morphologies is selectively examined using a previously developed 3D cold start model [37]. Next, the theoretical and simulation results are highlighted and comprehensively explained. Finally, recommendations to improve the cold start capability of PEMFCs are proposed.

2   Mesoscopic pore-scale morphology in CL

The membrane electrode assembly (MEA) is the critical and central part of PEMFC, which usually contains the Nafion membrane sandwiched by two catalyst layers serving as anodic and cathodic electrodes. The catalyst layer, in which the ECR, either the hydrogen oxidation reaction (HOR) in anode or the oxygen reduction reaction (ORR) in cathode, takes place, is commonly composed of three-phase transport, namely, a polyelectrolyte ionic conductive phase, a catalyst electronic phase, and a reagent/product transport pore phase. The ECRs only occur at active catalysts sites, where the catalyst phase, polyelectrolyte phase, and pore phase provide pathways for electron, ion, and reagent transport, respectively, i.e., the so-called triple-phase interface (TPI). The mesoscopic morphology in CL may have a great influence on the cold start of PEMFC.

The composition of the composite CL can be easily determined by experimental measurement and analysis in terms of the materials used in the preparation of CL, whereas the inside morphology of CL is generally very hard to be experimentally characterized due mainly to the

nano-scaled component and configuration. The presumed mesoscopic morphology inside CL is schematically demonstrated in Fig. 1. The catalystic phase usually contains Pt particles and carbon grains. Clusters of Pt/C grains covered by polyelectrolyte, commonly ionomer thin film, form agglomerates. Inside the agglomerate are small primary pores and in-between the agglomerates are large secondary pores. There are at least four distinct length scales: ① the thickness of CL is around 10 μm (along the through-plane x direction); ② the secondary pores are about 50–1000 nm; ③ the size of carbon grains is about 40 nm, that can be comparable to the size of primary pores, about 30–70 nm; ④ the size of Pt particles is approximately 3 nm, comparable to the thickness of the ionomer film [36,38–40].
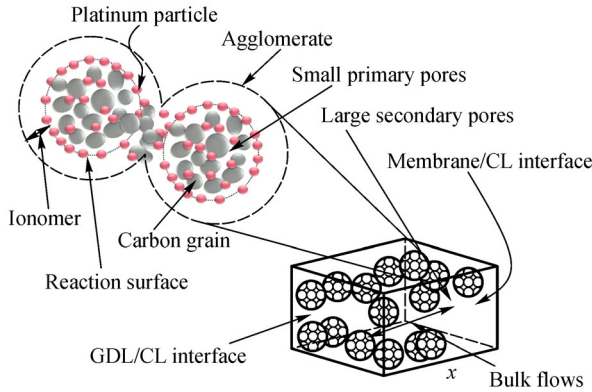

Fig. 1 Schematic of mesoscopic morphology in CL.

The microstructure inside CL must suffice each phase to have a good connectivity so that there are through-paths for the corresponding transport. The effective transport property (D^{eff}) of a phase in CL is its intrinsic transport property (D^0) multiplied by the component volume fraction (ε) and divided by the tortuosity (τ) of the transport paths, namely

$$D^{\text{eff}} = D^0 \frac{\varepsilon}{\tau}. \tag{1}$$

The D^0 can be the water diffusivity in membrane, membrane protonic conductivity, electronic conductivity in Pt/C phase, or gas diffusivity in pore phase. For gas phase (i.e., water vapor or a gaseous reactant) transport in pore space, as the size of pores, particularly the small primary pores, may be comparable to the mean free path of gas molecules, the Knudsen diffusion may play some role in the transport. Assuming the Knudsen diffusion is in parallel to the molecular diffusion, the intrinsic diffusivity of gas phase D_{g}^0 is calculated by [20]

$$D_{\text{g}}^0 = D_{\text{Kn}} + D_{\text{Nor}}, \tag{2}$$

where D_{Nor} denotes the normal molecular diffusivity and D_{Kn} the Knudsen diffusivity, which is calculated by [41]

$$D_{\text{Kn}} = \frac{1}{3}\left(\frac{8RT}{\pi M}\right)^{\frac{1}{2}} d_{\text{pore}}, \tag{3}$$

where M is the molecular weight of the gas, R the universal gas constant, T the temperature in Kelvin degree, and d_{pore} the pore size. D_{Kn} is commonly one to two orders of magnitude smaller than the D_{Nor}, i.e., $D_{\text{g}}^0 \approx D_{\text{Nor}}$. To achieve a better cold start capability for PEMFCs, novel preparation methods, which can create primary pores of larger size, may be desirable. Moreover, given the composition of CL, the tortuosity is the most proper parameter representing the mesoscopic morphology in CL.

The tortuosity (τ) can be related to the component volume fraction (ε) as

$$\tau = \varepsilon^{1-n}, \tag{4}$$

where the constant n stands for the Bruggeman coefficient [42], the magnitude of which reflects how tortuous the corresponding phase is. The larger the n, the more tortuous is the phase in CL.

3 Analysis of water transport in CCL during PEMFC cold start

Water flow plays a central role in dictating the fate of PEMFC cold start operations. Focusing on the CCL, where the ORR produces water, Jiang et al. [37] analyzed the water flow in PEMFC during cold start and obtained an overall water balance formula as

$$n_{\text{pro}} + n_{\text{CCL}} + n_{\text{MEM}} + n_{\text{anode}} + n_{\text{ice}} + n_{\text{outflow}} = 0. \tag{5}$$

In the left-hand side of Eq. (5), from the left to right, the terms denote the water production rate in CCL by the ORR (n_{pro}), the water uptake rate by the ionomers in CCL (n_{CCL}), the water absorption rate by the PEM (n_{MEM}), the water accumulation rate in anode (n_{anode}), the ice formation rate in the CCL/GDL (n_{ice}), and the water emission rate along with the exhaust gas flows (n_{outflow}), respectively. Moreover, n_{pro} is assigned a positive sign and n_{CCL}, n_{ice}, and n_{outflow} are always with negative values as they carry away the byproduct water produced. In the membrane (or anode), if the water back diffusion dominates over the electroosmotic drag (EOD), the water content variation, n_{MEM} (or n_{anode}) takes a negative value, otherwise a positive value is considered. Mathematically, all the quantities in Eq. (5) can be determined by

$$n_{\text{pro}} = \frac{M^{\text{H}_2\text{O}}}{A} \int_{V,\text{CCL}} -\frac{j}{2F} dV, \tag{6}$$

$$n_{\text{CCL}} = -\frac{M^{\text{H}_2\text{O}}}{A} \frac{\dfrac{\rho_{\text{MEM,dry}} \varepsilon_{\text{MEM}}}{\text{EW}} \int_{V,\text{CCL}} (\lambda|_{t+\Delta t} - \lambda|_t) dV}{\Delta t}, \tag{7}$$

$$n_{\text{MEM}} = -\frac{M^{\text{H}_2\text{O}}}{A}\frac{\dfrac{\rho_{\text{MEM,dry}}}{\text{EW}}\displaystyle\int_{V,\text{MEM}}(\lambda|_{t+\Delta t}-\lambda|_t)\text{d}V}{\Delta t}, \quad (8)$$

$$n_{\text{anode}} = -\frac{M^{\text{H}_2\text{O}}}{A}\frac{\dfrac{\rho_{\text{MEM,dry}}\varepsilon_{\text{MEM}}}{\text{EW}}\displaystyle\int_{V,\text{ACL}}(\lambda|_{t+\Delta t}-\lambda|_t)\text{d}V}{\Delta t}, \quad (9)$$

$$n_{\text{ice}} = -\frac{M^{\text{H}_2\text{O}}}{A}\int_{V,\text{CCL\&GDL}}\dot{q}_{gs}^{\text{H}_2\text{O}}\text{d}V, \quad (10)$$

$$n_{\text{outflow}} = -\frac{M^{\text{H}_2\text{O}}}{A}\int_{A,\text{outlets}}C^{\text{H}_2\text{O}}u_{\text{out}}\text{d}A. \quad (11)$$

Note that all the rate quantities are multiplied by a factor of $M^{\text{H}_2\text{O}}/A$ to have a unit of $\text{kg}\cdot\text{m}^{-2}\cdot\text{s}^{-1}$. In Eqs. (6–11), j is the transfer current density; F is the Faraday constant; A is the side surface area of the bipolar plate; the notation t is used to denote time; λ indicates the water content; $\rho_{\text{MEM,dry}}$ is the density of dry membrane; EW is the equivalent weight of membrane; $\dot{q}_{gs}^{\text{H}_2\text{O}}$ stands for the phase change rate per unit of volume; $C^{\text{H}_2\text{O}}$ represents the water vapor concentration; μ_{out} signifies the outlet velocity; $\int \text{d}V$ correspond to the volume integration over selected domain, and $\int \text{d}A$ denotes the area integration over certain surface.

The water transport in CCL is of paramount importance to the cold start of PEMFCs. The water transport resistance in CCL will affect the water back diffusion, meaning the two terms: n_{MEM} and n_{anode} in Eq. (5) will be directly influenced. The water transport in CL relies on two mechanisms: water vapor transport through the pores and water transport in the ionomer phase. The ratio of the water back diffusion flux due to the vapor transport in pores ($\psi_g^{\text{H}_2\text{O}}$) to that due to the water transport in ionomer phase
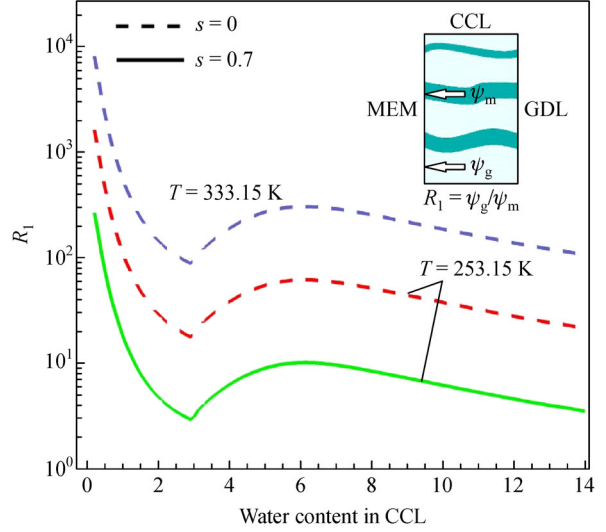
Fig. 2 Dependence of R_1 on cell temperature and the water content and ice fraction in CCL.

($\psi_m^{\text{H}_2\text{O}}$) is defined as R_1, which can be expressed as

$$R_1 = \frac{\psi_g^{\text{H}_2\text{O}}}{\psi_m^{\text{H}_2\text{O}}} = \frac{D_g^{\text{H}_2\text{O}}[\varepsilon_0(1-s)]^{\tau_g}(C_{\text{H}_2\text{O,CCL}}-C_{\text{H}_2\text{O,MEM}})}{D_{\text{MEM}}^{\text{H}_2\text{O}}\varepsilon_{\text{MEM}}^{\tau_m}(\lambda_{\text{CCL}}-\lambda_{\text{MEM}})\dfrac{\rho_{\text{MEM,dry}}}{\text{EW}}}, \quad (12)$$

where $D_g^{\text{H}_2\text{O}}$ and $D_{\text{MEM}}^{\text{H}_2\text{O}}$ denote the water vapor diffusivity and the water diffusivity in PEM, respectively; ε_0 and ε_{MEM} are the porosity and membrane content in CCL, respectively; τ_g and τ_m are the tortuosity for the pore and ionomer phase in CCL, respectively; s the ice fraction in CCL pore space.

$D_{\text{MEM}}^{\text{H}_2\text{O}}$ is a function of the water content in membrane phase and the temperature, and $D_g^{\text{H}_2\text{O}}$ is also dependent on the temperature, as in Refs. [34,37].

$$D_{\text{MEM}}^{\text{H}_2\text{O}} = \begin{cases} 5.93\times10^{-5}\lambda(\exp(0.28\lambda)-1)\exp\left(\dfrac{-4269}{T}\right), & \text{for } 0<\lambda\leqslant3, \\[3mm] 7.97\times10^{-6}\lambda(1+161\exp(-\lambda))\exp\left(\dfrac{-4269}{T}\right), & \text{otherwise,} \end{cases} \quad (13)$$

$$D_g^{\text{H}_2\text{O}} = D_0\left(\frac{T}{353.15}\right)^{\frac{3}{2}}\left(\frac{p_0}{p}\right). \quad (14)$$

Considering a typical cell design with $\varepsilon_0 = 0.53$, $\varepsilon_{\text{MEM}} = 0.15$, and assuming $\tau_g = \tau_m = 1.5$ and an extreme case with zero water content and zero vapor concentration in PEM, the R_1 values are calculated and the results are presented in Fig. 2. At normal operation temperatures ($T > 333.15$ K), R_1 is more than 100, whereas at subfreezing temperatures,

it is at least one order of magnitude smaller. The formed ice at subfreezing temperatures further decreases the R_1 value. During PEMFC cold start, when a large quantity of ice is present in the CCL, the water transport through ionomer may play an equally important role as compared to the vapor diffusion in CCL pores.

The ice formed in the CCL can potentially block the reactants transport or may cover the area where the ECRs occur. Consequently, enhancing the water removal from the CCL can be very beneficial for improving the cold start

performance. The water back diffusion from the CCL to the anode side needs to overcome the transport resistance in CCL and that in the PEM. To compare the water transport resistance in CCL and in PEM, denoted by r_{CCL} and r_{MEM}, respectively, a new parameter R_2 is defined as

$$R_2 = \frac{r_{MEM}}{r_{CCL}} = \frac{\delta_{MEM}}{D_{MEM}^{H_2O} \dfrac{\rho_{MEM,dry}}{EW} \dfrac{RT}{p_{sat}} \dfrac{d\lambda}{da}} \Bigg/$$

$$\frac{\dfrac{\delta_{CCL}}{2}}{[\varepsilon_0(1-s)]^{\tau_g} D_g^{H_2O} + \varepsilon_{MEM}^{\tau_m} D_{MEM}^{H_2O} \dfrac{\rho_{MEM,dry}}{EW} \dfrac{RT}{p_{sat}} \dfrac{d\lambda}{da}} \quad (15)$$

where δ_{MEM} and δ_{CCL} denote the thickness of PEM and CCL, respectively; p_{sat} is the saturated vapor pressure in CCL, and a is the water activity.

Likewise, considering a typical cell design with $\varepsilon_0 = 0.53$, $\varepsilon_{MEM} = 0.15$, $\delta_{MEM} = 30$ μm, $\delta_{CCL} = 10$ μm, and assuming $\tau_g = \tau_m = 1.5$, the R_2 values are calculated and the results are presented in Fig. 3. The water transport resistance in PEM can be hundreds of times of that in CCL at normal operation temperatures, whereas at subfreezing temperatures, especially when the PEM is more hydrated and large quantity of ice is present, the water
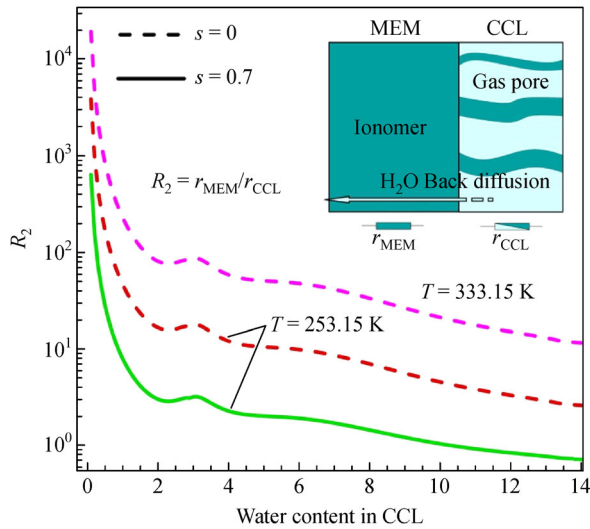
transport resistance in CCL can be comparable to that in PEM. Therefore, lowering the water transport resistance in the CCL should be effective to promote the PMEFC cold start ability.

4 Effects of CCL mesoscopic morphology

A wide range of tortuosity values has been reported in the literature considering varied calculation approaches such as Bruggeman equation and lattice Boltzmann modeling [43]. It is worth pointing out that in the pore-scale lattice Boltzmann modeling by Wu and Jiang [36], the τ_m and τ_g are determined to be 2.18 and 3.11, respectively.

To get more details about the effects of CCL mesoscopic morphology on PEMFC cold start, 3D numerical simulations are performed, as shown in Table 1. Four cases are defined to investigate the effects of CCL mesoscopic morphology on PEMFC cold start from subfreezing temperature.

4.1 Numerical model

The present study is based on a three-dimensional, non-isothermal, multiphase, transient PEMFC model that has been previously developed by Jiang et al. [37]. A brief description of the model is first presented in this subsection, while the detailed cold start modeling description can be found in Refs. [37,44,45]. In this model it is assumed that the gravity effect is neglected. All the gas species obey the ideal gas law. The flow is laminar due to the small pressure gradient. The fluid is incompressible due to the small pressure gradients in flows. The GDLs and CLs are considered as isotropic and homogeneous porous layers. For the CL and GDL, there is no liquid water existing but a direct phase transition from vapor water to solid ice [10,46,47].

Therefore, the phase change source term (S_{ice}) in water conservation equation can be calculated as

Fig. 3 Dependence of R_2 on cell temperature and the water content and ice fraction in CCL.

$$S_{ice} = \begin{cases} 0, & C^{H_2O} \leqslant C_{sat}^{H_2O}, \\ r_{freeze}(C_{sat}^{H_2O} - C^{H_2O}), & C^{H_2O} > C_{sat}^{H_2O} \text{ and } T < T_{freeze}^{H_2O}, \\ r_{melt}(C_{sat}^{H_2O} - C^{H_2O}), & T = T_{freeze}^{H_2O} \text{ and } s > 0, \\ 0, & T \geqslant T_{freeze}^{H_2O} \text{ and } s = 0, \end{cases}$$

$$(16)$$

Table 1 Simulation cases

Cases	Tortuosity		Note
	τ_m	τ_g	
Case 1	1.5	1.5	Both the ionomer network and pore structure in CLs are less tortuous
Case 2	2.5	2.5	Both the ionomer network and pore structure in CLs are tortuous
Case 3	2.5	1.5	The ionomer network is tortuous, while the pore structure in CLs is less tortuous
Case 4	1.5	2.5	The ionomer network is less tortuous, while the pore structure in CLs is tortuous

where r_{freeze} and r_{melt} are phase change rates for freezing and melting, respectively.

The current collector at the anode side is set to electric ground (0 V) and at the cathode side to a constant flux (current density) [21].

The model can be concisely summarized through the following governing equations, which basically describe the five principles of conservation.

Mass continuity equation

$$\frac{\partial(\varepsilon_{\text{s}}\rho_{\text{s}})}{\partial t} + \frac{\partial(\varepsilon\rho)}{\partial t} + \nabla\cdot\left(\rho\,\vec{u}\right) = 0. \qquad (17)$$

Momentum conservation equation

$$\frac{\partial(\rho\,\vec{u}\,/\varepsilon)}{\partial t} + \nabla\cdot\left(\frac{\rho\,\vec{u}\,\vec{u}}{\varepsilon^2}\right)$$
$$= \nabla\cdot\left(\mu\nabla\,\vec{u}\right) - \nabla p + S_u. \qquad (18)$$

Species conservation equation

$$\frac{\partial(\varepsilon C^w)}{\partial t} + \nabla\cdot\left(\vec{u}\,C^w\right) = \nabla\cdot(D_{\text{eff}}^w\nabla C^w) + S_v^w. \qquad (19)$$

Charge conservation for electrons

$$0 = \nabla\cdot(\sigma_{\text{solid}}^{\text{eff}}\nabla\varphi_{\text{solid}}) + S_{\varphi_{\text{solid}}}. \qquad (20)$$

Charge conservation for protons

$$0 = \nabla\cdot(\kappa_{\text{e}}^{\text{eff}}\nabla\varphi_{\text{e}}) + S_{\varphi_{\text{e}}}. \qquad (21)$$

Energy conservation equation

$$\frac{\partial[(\rho c_p)_{\text{cell}}T]}{\partial t} + \nabla\cdot\left[\rho c_p\,\vec{u}\,T\right] = \nabla\cdot(k_{\text{eff}}\nabla T) + S_T. \qquad (22)$$

The porosity ε in the above equations becomes unity in the gas channel, while in porous layers it is a variable depending on the intrinsic porosity ε_0 and the local ice fraction s, namely, $\varepsilon = \varepsilon_0(1-s)$. The volume fractions occupied by ice and by the solid matrix can be expressed as

$\varepsilon_{\text{s}} = \varepsilon_0 s$ and $\varepsilon_{\text{m}} = 1-\varepsilon_0$, respectively. $\vec{u}$ and μ denote the superficial fluid velocity vector and fluid viscosity, respectively. Effective transport coefficients D_{eff}, $\sigma_{\text{s}}^{\text{eff}}$, and $\kappa_{\text{e}}^{\text{eff}}$ are modified in terms of the Bruggeman theorem, as expressed in Eq. (1). The fluid relative permeability K in porous layers is assumed to follow a cubic relation to the ice fraction s, i.e., $K = K_0 (1-s)^3$. The source terms in conversation equations for momentum (S_u), species (S_v), electrons charge ($S_{\varphi_{\text{solid}}}$), protons charge ($S_{\varphi_{\text{e}}}$), and energy ($S_T$) in each sub-region are listed in Table 2, and the relevant material and transport properties are summarized in Table 3 [37], in which U_{o} represents the equilibrium cell potential, i is the exchange current density, η is the activation overpotential, and h_{gs} denotes the latent heat of vapor desublimation.

The geometry of the simulated unit cell and its numerical mesh are presented in Fig. 4. The geometry considers nine sub-regions: membrane, anode flow channel, anode GDL, anode catalyst layer (ACL), anode bipolar plate, cathode flow channel, cathode GDL, CCL, cathode bipolar plate. L_x, L_y, L_z are the width, length, and height of the simulated cell, respectively; X and Y represent the distance in the thru-plane and in-plane directions, respectively.

The cell dimensions and operating conditions are given in Table 4. Based on the experiment performed by Bradean et al. [48], the initial ice fraction and initial water content in CCL and membrane are defined to be independent on the location along the flow direction as

$$s_0 = \begin{cases} 0, & (Y/L_y < 1/6), \\ 0.3\left[1-\exp\left(-\dfrac{Y-0.1}{0.05}\right)\right], & (Y/L_y \geqslant 1/6), \end{cases} \qquad (23)$$

$$\lambda_0 = \begin{cases} 1.4, & (Y/L_y < 1/6), \\ 5.4\left(\dfrac{Y}{L_y}\right) + 0.5, & (1/6 \leqslant Y/L_y \leqslant 5/6), \\ 5.0, & (Y/L_y > 5/6). \end{cases} \qquad (24)$$

Figure 5 illustrates the initial water content in the

Table 2 Source terms for conversation equations

Source term	Gas channels	GDLs	Catalyst layers	Membrane
S_u	0	$-\dfrac{\mu}{K_{\text{GDL}}}\vec{u}$	$-\dfrac{\mu}{K_{\text{CL}}}\vec{u}$	–
$S_v^{\text{H}_2\text{O}}$	0	$-\dot{q}_{\text{gs}}^{\text{H}_2\text{O}}$	$-\nabla\cdot\left(\dfrac{n_d}{F}i_{\text{e}}\right) - \dfrac{S_v j}{nF} - \dot{q}_{\text{gs}}^{\text{H}_2\text{O}}$	$-\nabla\cdot\left(\dfrac{n_d}{F}i_{\text{e}}\right)$
S_v (for reactants)	0	0	$-\dfrac{S_v j}{nF}$	0
$S_{\varphi_{\text{e}}}$	–	–	j	0
$S_{\varphi_{\text{solid}}}$	0	0	$-j$	–
S_T	–	$\dfrac{i_{\text{solid}}^2}{\sigma_{\text{solid}}^{\text{eff}}} + \dot{q}_{\text{gs}}^{\text{H}_2\text{O}}h_{\text{gs}}$	$j\left(\eta - T\dfrac{\partial(U_{\text{o}})}{\partial T}\right) + \dfrac{i_{\text{e}}^2}{\kappa_{\text{e}}^{\text{eff}}} + \dfrac{i_{\text{solid}}^2}{\sigma_{\text{solid}}^{\text{eff}}} + \dot{q}_{\text{gs}}^{\text{H}_2\text{O}}h_{\text{gs}}$	$\dfrac{i_{\text{e}}^2}{\kappa_{\text{e}}^{\text{eff}}}$

Table 3 Cell and transport properties

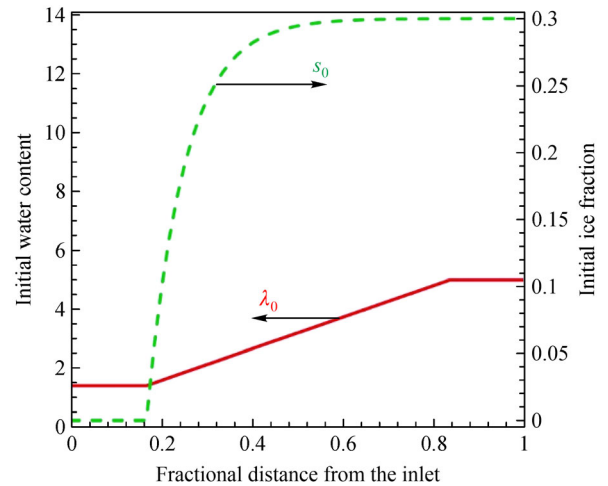| Description	Value
Porosity of GDL	0.6
Porosity of CL (initial)	0.53
Volume fraction of ionomer in CL	0.15
Density of gas mixture/(kg·m^{-3})	1
Heat capacity of membrane, CL, GDL, bipolar plate/(kJ·m^{-3}·K^{-1})	1650, 3300, 568, 1580
Heat conductivity of membrane, CL, GDL, bipolar plate/(W·m^{-1}·K^{-1})	0.95, 1, 1, 20
Heat capacity of ice, frost/ (kJ·m^{-3}·K^{-1})	3369.6
Heat conductivity of ice, frost/(W·m^{-1}·K^{-1})	2.4
Latent heat of desublimation/(J·mol^{-1})	5.1×10^4
Permeability of CL/m^2	1×10^{-13}
Electronic conductivity of GDL, CL, bipolar plate/(S·m^{-1})	300, 300, 1×10^7
Equivalent weight of ionomer/(kg·mol^{-1})	1.1
Density of dry membrane/(kg·m^{-3})	1980
H$_2$/H$_2$O diffusivity in anode/(m^2·s^{-1})	8.67×10^{-5}, 8.67×10^{-5}
O$_2$/H$_2$O diffusivity in cathode/(m^2·s^{-1})	1.53×10^{-5}, 1.79×10^{-5}
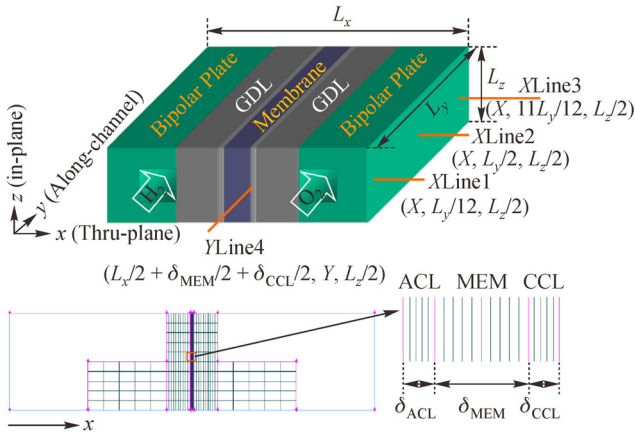
Fig. 4 Geometry and numerical mesh of simulated cell (Positions of 4 monitoring lines (XLine1, XLine2, XLine3, and YLine4) are annotated. These four lines will be used to illustrate the simulation results.)

Fig. 5 Profiles of initial water content (in the membrane/CL) and initial ice fraction (in CL/GDL) before cold start.

membrane and CLs, and the initial ice fraction in CCL. Initially, the cell is in the 253.15 K thermally-static state and is started up by imposing a 100 mA·cm^{-2} current load at the side surface of the cathode current collector. The numerical procedure including the grid-independence examination has been detailed in Ref. [37] and thus is not repeated here.

4.2 Results and discussion

First, the calculated results of Cases 1 and 2 are presented and compared. Figure 6 compares the distributions of effective water diffusivity and water content in the membrane and CCL along the three monitoring lines: XLine1, XLine2, and XLine3, at time instants of 4 s and 38 s. Even at the very early time, 4 s, it can be observed that slightly more water is stored in the membrane and less water is accumulated in the CCL for the cold start case (Case 1) with the CCL of less tortuous mesoscale morphology. More tortuous mesoscale morphology increases the water diffusive resistance in the CCL and the water back diffusion from the CCL to the membrane is thus constrained. At a later time, 38 s, the water transported inside the membrane from the CCL is distinctively more sufficient for the case (Case 1) with the CCL of less tortuous mesoscale morphology. From Fig. 6, it can also be

Table 4 Cell dimensions and operating conditions

Description	Value
Cell height, length/mm	2, 600
Land shoulder width/mm	1
Anode, cathode GDL thickness/μm	300, 300
Anode/cathode CL thickness/μm	10, 10
Membrane thickness/μm	30
Channel depth, width/mm	1, 1
Initial water content	6.2
Startup temperature/K	253.15
Current density/(mA·cm^{-2})	100
Anode/cathode stoichiometry	2
Anode/cathode inlet gas temperature/K	253.15
Anode/cathode pressure "absolute"/Pa	1.01×10^5

observed that the effective water diffusivity in the CCL is of the same order of magnitude as that in the membrane, in accordance with the analysis in Fig. 3. This accounts for the fact that modifying the mesoscale morphology in the CCL can effectively influence the water back diffusion process.

Figure 7 exhibits the water balance map of Cases 1 and 2 during the cold start process. The positive and negative values represent water generation and water removal from (or water consumption in) CCL, respectively. Membrane water uptake rate during the cold start for Case 1 (Fig. 7(a)) is faster and the ice formation rate is slower, as displayed in the overall water balance maps. For Case 2 (Fig. 7(b)), in which the CCL is of more tortuous mesoscale morphology, partial shutdown at the cell near the gas channel outlet portion occurs at the time of around 40 s, which further decreases the membrane water uptake rate and promotes
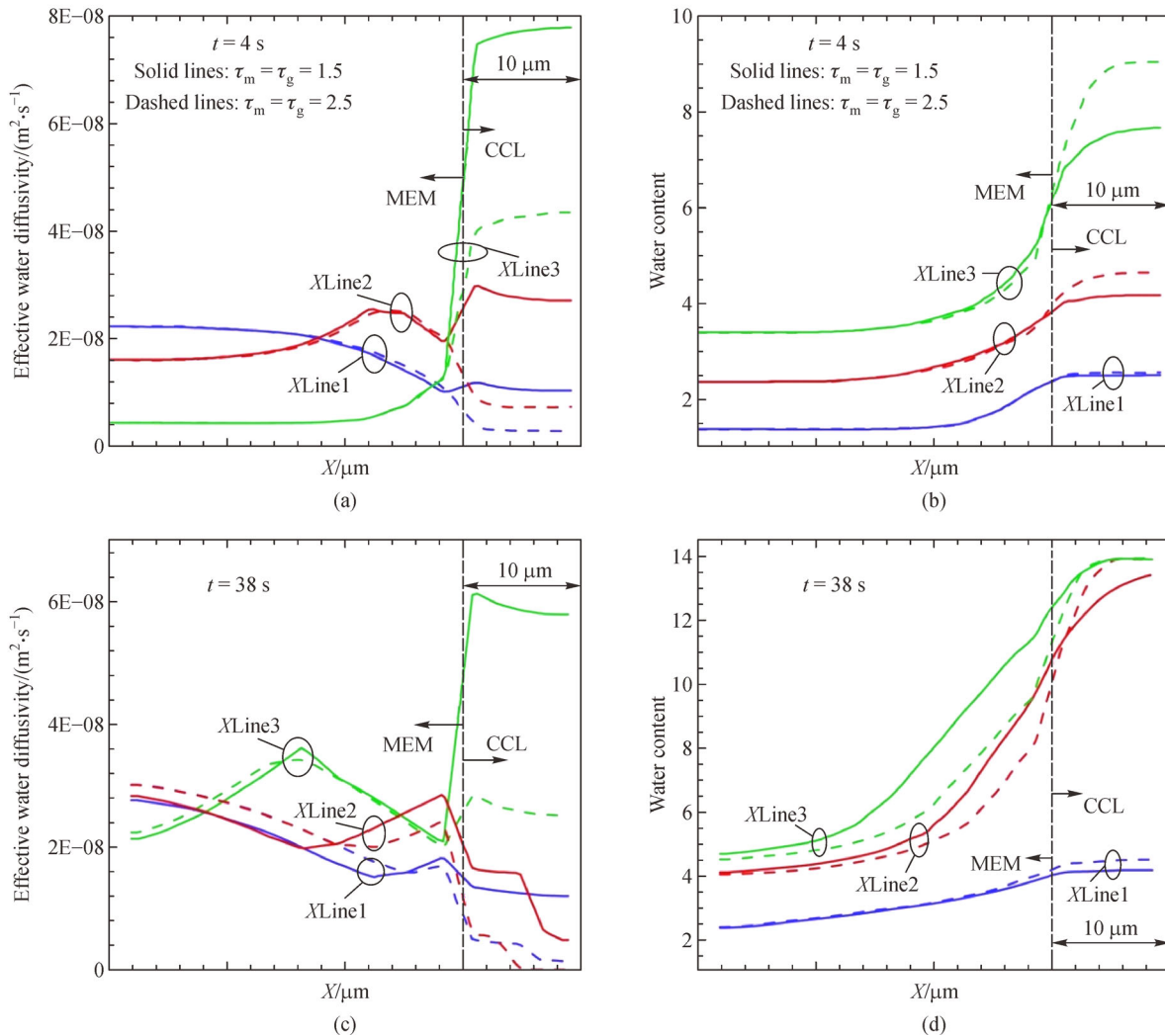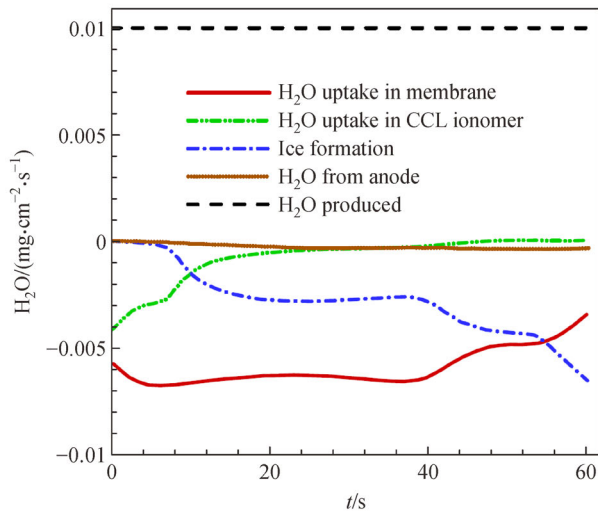

Fig. 6 Profiles of effective water diffusivity, and water content in membrane and CCL along XLine1, XLine2, and XLine3: a comparison of Case 1 and Case 2 at two time instants, 4 s and 38 s.
(a) Effective water diffusivity profile at $t = 4$ s; (b) water content profile at $t = 4$ s; (c) effective water diffusivity profile at $t = 38$ s; (d) water content profile at $t = 38$ s.
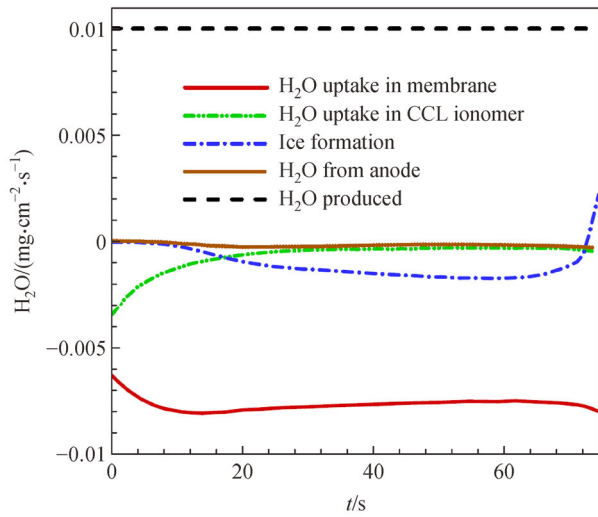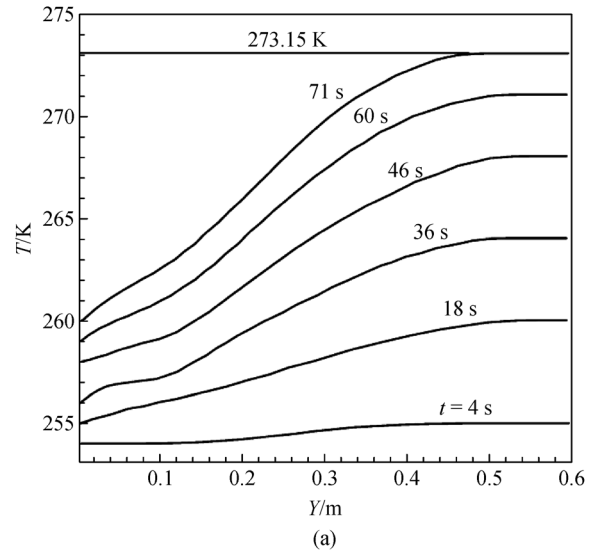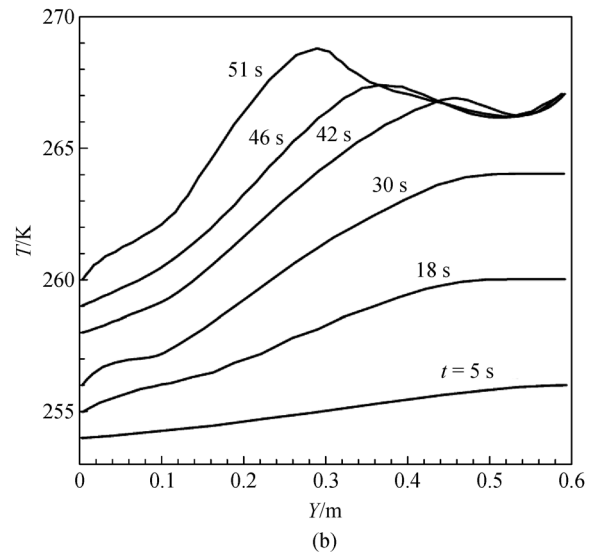
Fig. 7 Analysis of water flow in cell during cold start.
(a) Case 1; (b) Case 2.

Fig. 8 Temperature profile and its temporal-evolution in CCL along YLine 4.
(a) Case 1; (b) Case 2.

the ice formation. For the Case 1 cold start process, at time of about 70 s, ice formation rate changes its sign from a negative to a positive value, which means ice begins to melt as the temperature is elevated higher than 273.15 K (Fig. 8(a)) and a successful self-startup is expected subsequently. Case 2 shows a generally much faster ice formation rate than Case 1.

Figure 8 presents the comparison of temperature profiles along YLine4 in the CCL for Cases 1 and 2. For the cold start process with the CCL of less tortuous mesoscale morphology, i.e., Case 1, the highest temperature always locates at the channel outlet portion where the strongest ORR is occurring, and at the time of 71 s, it reaches the freezing point, 273.15 K, (Fig. 8(a)). For the cold start process with the CCL of more tortuous mesoscale morphology, i.e. Case 2, partial shutdown starts from the

cell near the channel outlet portion at time around 40 s, and the location of the highest temperature is thus observed to gradually shift from the cell channel outlet portion to an interior position (Fig. 8(b)). The highest temperature is still lower than 273.15 K at the time of 51 s, and the cell goes to shutdown (Fig. 9).

Figure 9 summarizes the cell voltage evolution curves for all the four cases simulated. It can immediately be observed is that the mesoscale morphology in the CCL does have a significant effect on the PEMFC cold start performance. Different CL morphologies can lead to different fates of a cold start operation. The cold start with the CCL of less tortuous mesoscale morphology (i.e., Cases 1 and 3) can start up, whereas that with the CCL of more tortuous mesoscale morphology (i.e., Cases 2 and 4) gets shutdown. Secondly, the effect of the ionomer
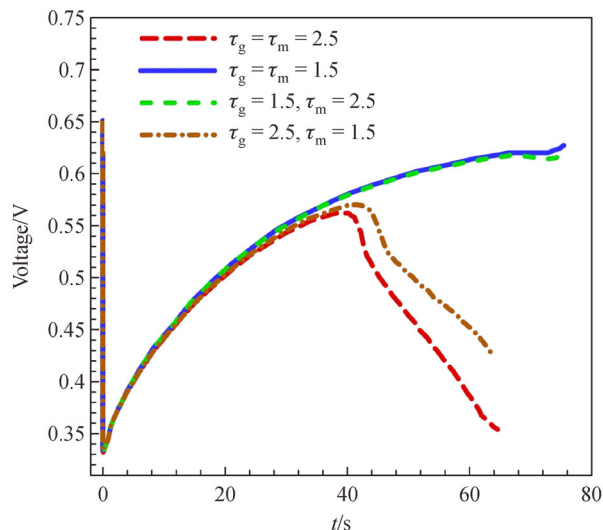
Fig. 9 Cell voltage curves for non-isothermal cold start from 253.15 K with different mesoscopic morphologies in CCL.

Fig. 10 Cell voltage evolutions for isothermal cold start from 253.15 K with different mesoscopic morphologies in CCL.

morphology on PEMFC cold start performance cannot be neglected, especially when the pore structure in the CCL is relatively tortuous and/or large quantity of ice is formed. This verifies the results obtained from the analysis conveyed in Section 3.

All the four cases simulated are non-isothermal. Hence, the CL morphology effect presented in Fig. 9 is actually compounded with the effect of the rising cell temperature. Both Figs. 2 and 3 indicate that the temperature can have a tremendous influence on the CL morphology at a high temperature. The CL morphology is of little effect on the water back diffusion from the CCL to the membrane, while at subfreezing temperatures, it may play a very important role in PEMFC cold start. To clarify the involved physics, four isothermal simulations with the same CL morphology parameters as used in the non-isothermal ones are performed. The isothermal cold start under the subzero operating condition describes an extreme situation, and the cold start is bound to shut down by ice formation as the cell temperature is fixed at the initial subzero temperature. However, it is frequently used to evaluate and understand the intrinsic cold start performance of PEMFCs [49–51]. Figure 10 plots the cell voltage evolution curves. In general, the CL morphology effect observed in isothermal cold start operations is more evident than that in non-isothermal ones. One reason for this is that the isothermal cold start excludes the rising cell temperature effect [37] in practical non-isothermal cold start operations. The other reason for this is that in isothermal cold start operations, the measured data are independent of the cell fixture and its thermal mass, but depends more on the intrinsic properties of the cell [48].
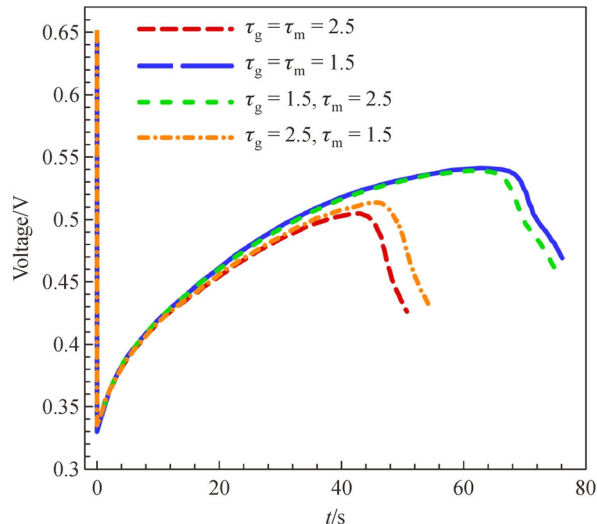
5   Conclusions

Enhancing the water back diffusion can accelerate water removal from the CCL and water storage in the membrane, which is thought to be an effective method to enhance the cold start performance of PEMFCs. The water back diffusion is greatly affected by the water transport in CLs. At subfreezing temperatures, due to the very low saturated-vapor pressure and the plugged-in pores by the formed ice/frost, vapor phase transport through pore space is not the sole dominant mechanism for water transport in CLs anymore.

Simplified theoretical analyses find that at subfreezing temperatures the water transport resistance in the CL is comparable to that in the membrane, and water transport through ionomer in the CL is as important as the water diffusion in gas phase. Simulations by using a previously developed PEMFC cold start model reveal more details about the CL morphology effects. Different CL morphology can lead to different fates of a cold start operation. Cold-starting a cell with a CCL of less tortuous mesoscale morphology can succeed, whereas starting up a cell with a CCL of more tortuous mesoscale morphology may fail.

Some clues are thus obtained for improving the cold start capability of PEMFCs, for instance, minimizing the tortuosity factors for both the pore space and the ionomer network. Tailoring the CCL to be of one-dimensional nanowire structure can lower the tortuosity factors to be approximately one, which may greatly enhance the self-cold startup capability of PEMFCs.

Notations

A	Side surface area of the bipolar plate/m^2
a	Water activity
c_p	Specific heat capacity/(J·kg^{-1}·K^{-1})
C	Species concentration/(mol·m^{-3})
D	Diffusivity/(m^2·s^{-1})
EW	Equivalent weight of dry membrane/(kg·mol^{-1})
F	Faraday's constant/(C·mol^{-1})
h	Latent heat/(J·mol^{-1})
i	Exchange current density/(A·m^{-2})
j	Transfer current density/(A·m^{-3})
K	Permeability/m^2
M	Molecular weight of gas
n	Bruggeman factor
n_d	Electroosmatic drag coefficient/(H$_2$O/H$^+$)
p	Pressure/Pa
$\dot{q}$	Water desublimation rate/(mol·m^{-3}·s^{-1})
R	Universal gas constant/(J·mol^{-1}·K^{-1})
r_{CCL}	Water transport resistance in CCL/(s·m^{-1})
r_{MEM}	Water transport resistance in membrane/(s·m^{-1})
S	Source term
s	Ice fraction
t	Time/s
T	Temperature/K
U_o	Equilibrium cell potential/V
u	Superficial fluid velocity/(m·s^{-1})
V	Cell voltage/V
x, y, z	Cartesian coordinates

Greek symbols

δ	Thickness/m
ε	Porosity
η	Activation overpotential/V
κ	Ionic conductivity/(S·m^{-1})
κ_D	Diffusional conductivity/(S·m^{-1})
λ	Water content/(mol H$_2$O/mol SO$_3^-$)
ρ	Density/(kg·m^{-3})
σ	Electronic conductivity/(S·m^{-1})
φ	Electric potential/V
μ	Viscosity/(Pa·s)
ϕ_e	Electrolyte potential/V
ϕ_s	Electron potential/V
τ	Tortuosity factor
ψ	Water back diffusion flux/(mol·m^{-2}·s^{-1})

Subscripts/Superscripts

e	Electrolyte
eff	Effective
g	Vapor phase
gs	Vapor-solid phase transition
Kn	Knudsen
m	ionomer phase
MEM	Membrane
Nor	Normal
0	Initial
s	Ice or solid phase
sat	Saturated
solid	Solid phase
v	Species index
w	Component (hydrogen, oxygen, or water)
-	Average
$\rightarrow$	Vector

References

1. Tai X Y, Zhakeyev A, Wang H, et al. Accelerating fuel cell development with additive manufacturing technologies: state of the art, opportunities and challenges. Fuel Cells (Weinheim), 2019, 19 (6): 636–650

2. Zhang T, Wang P, Chen H, et al. A review of automotive proton exchange membrane fuel cell degradation under start-stop operating condition. Applied Energy, 2018, 223: 249–262

3. Ajanovic A, Haas R. Economic and environmental prospects for battery electric- and fuel cell vehicles: a review. Fuel Cells (Weinheim), 2019, 19(5): 515–529

4. Dafalla A M, Jiang F M. Stresses and their impacts on proton exchange membrane fuel cells: a review. International Journal of Hydrogen Energy, 2018, 43(4): 2327–2348

5. Pan W, Li P, Gan Q, et al. Thermal stability analysis of cold start processes in PEM fuel cells. Applied Energy, 2020, 261: 114430

6. Huo S, Jiao K, Park J W. On the water transport behavior and phase transition mechanisms in cold start operation of PEM fuel cell. Applied Energy, 2019, 233–234: 776–788

7. Luo Y, Jiao K. Cold start of proton exchange membrane fuel cell. Progress in Energy and Combustion Science, 2018, 64: 29–61

8. Amamou A A, Kelouwani S, Boulon L, et al. A Comprehensive review of solutions and strategies for cold start of automotive proton exchange membrane fuel cells. IEEE Access: Practical Innovations, Open Solutions, 2016, 4: 4989–5002

9. Shojaeefard M H, Molaeimanesh G R, Nazemian M, et al. A review on microstructure reconstruction of PEM fuel cells porous electrodes for pore scale simulation. International Journal of Hydrogen Energy, 2016, 41(44): 20276–20293

10. Ko J, Ju H. Comparison of numerical simulation results and experimental data during cold-start of polymer electrolyte fuel cells. Applied Energy, 2012, 94: 364–374

11. Gwak G, Ko J, Ju H. Effects of porous properties on cold-start behavior of polymer electrolyte fuel cells from sub-zero to normal operating temperatures. Scientific Reports, 2015, 4(1):5770

12. Li L, Wang S, Yue L, et al. Cold-start icing characteristics of proton-exchange membrane fuel cells. International Journal of Hydrogen Energy, 2019, 44(23): 12033–12042

13. Cetinbas F C, Ahluwalia R K, Kariuki N N, et al. Effects of porous carbon morphology, agglomerate structure and relative humidity on local oxygen transport resistance. Journal of the Electrochemical Society, 2020, 167(1): 013508

14. Ozden A, Shahgaldi S, Li X, et al. The impact of ionomer type on the morphological and microstructural degradations of proton exchange membrane fuel cell electrodes under freeze-thaw cycles. Applied Energy, 2019, 238: 1048–1059

15. Shahgaldi S, Ozden A, Li X, et al. Cathode catalyst layer design with gradients of ionomer distribution for proton exchange membrane fuel cells. Energy Conversion and Management, 2018, 171: 1476–1486

16. Shahgaldi S, Alaefour I, Li X. Impact of manufacturing processes on proton exchange membrane fuel cell performance. Applied Energy, 2018, 225: 1022–1032

17. Zhao J, Ozden A, Shahgaldi S, et al. Effect of Pt loading and catalyst type on the pore structure of porous electrodes in polymer electrolyte membrane (PEM) fuel cells. Energy, 2018, 150: 69–76

18. Wu H W. A review of recent development: transport and performance modeling of PEM fuel cells. Applied Energy, 2016, 165: 81–106

19. Heidary H, Jafar Kermani M, Khajeh-Hosseini-Dalasm N. Performance analysis of PEM fuel cells cathode catalyst layer at various operating conditions. International Journal of Hydrogen Energy, 2016, 41(47): 22274–22284

20. Wang C Y. Fundamental models for fuel cell engineering. Chemical Reviews, 2004, 104(10): 4727–4766

21. Jiang F M, Wang C Y. Numerical modeling of liquid water motion in a polymer electrolyte fuel cell. International Journal of Hydrogen Energy, 2014, 39(2): 942–950

22. Sabharwal M, Pant L M, Patel N, et al. Computational analysis of gas transport in fuel cell catalyst layer under dry and partially saturated conditions. Journal of the Electrochemical Society, 2019, 166(7): F3065–F3080

23. Hou Y, Deng H, Pan F, et al. Pore-scale investigation of catalyst layer ingredient and structure effect in proton exchange membrane fuel cell. Applied Energy, 2019, 253: 113561

24. Molaeimanesh G R, Akbari M H. Agglomerate modeling of cathode catalyst layer of a PEM fuel cell by the lattice boltzmann method. International Journal of Hydrogen Energy, 2015, 40(15): 5169–5185

25. Moein-Jahromi M, Kermani M J. Performance prediction of PEM fuel cell cathode catalyst layer using agglomerate model. International Journal of Hydrogen Energy, 2012, 37(23): 17954–17966

26. Weber A Z, Borup R L, Darling R M, et al. A critical review of modeling transport phenomena in polymer-electrolyte fuel cells. Journal of the Electrochemical Society, 2014, 161(12): F1254–F1299

27. Sassin M B, Garsany Y, Atkinson R W III, et al. Understanding the interplay between cathode catalyst layer porosity and thickness on transport limitations en route to high-performance PEMFCs. International Journal of Hydrogen Energy, 2019, 44(31): 16944–16955

28. Carcadea E, Varlam M, Marinoiu A, et al. Influence of catalyst structure on PEM fuel cell performance: a numerical investigation. International Journal of Hydrogen Energy, 2019, 44(25): 12829–12841

29. Molaeimanesh G R, Bamdezh M A, Nazemian M. Impact of catalyst layer morphology on the performance of PEM fuel cell cathode via lattice Boltzmann simulation. International Journal of Hydrogen Energy, 2018, 43(45): 20959–20975

30. Nandy A, Jiang F M, Ge S, et al. Effect of cathode pore volume on PEM fuel cell cold start. Journal of the Electrochemical Society, 2010, 157(5): B726–B736

31. Luo Y, Jia B, Jiao K, et al. Catalytic hydrogen-oxygen reaction in anode and cathode for cold start of proton exchange membrane fuel cell. International Journal of Hydrogen Energy, 2015, 40(32): 10293–10307

32. Hiramitsu Y, Mitsuzawa N, Okada K, et al. Effects of ionomer content and oxygen permeation of the catalyst layer on proton exchange membrane fuel cell cold start-up. Journal of Power Sources, 2010, 195(4): 1038–1045

33. Xie X, Zhang G, Zhou J, et al. Experimental and theoretical analysis of ionomer/carbon ratio effect on PEM fuel cell cold start operation. International Journal of Hydrogen Energy, 2017, 42(17): 12521–12530

34. Ko J, Ju H. Effects of cathode catalyst layer design parameters on cold start behavior of polymer electrolyte fuel cells (PEFCs). International Journal of Hydrogen Energy, 2013, 38(1): 682–691

35. He P, Chen L, Mu Y T, et al. Lattice Boltzmann method simulation of ice melting process in the gas diffusion layer of fuel cell. International Journal of Heat and Mass Transfer, 2020, 149: 119121

36. Wu W, Jiang F M. Microstructure reconstruction and characterization of PEMFC electrodes. International Journal of Hydrogen Energy, 2014, 39(28): 15894–15906

37. Jiang F M, Fang W, Wang C Y. Non-isothermal cold start of polymer electrolyte fuel cells. Electrochimica Acta, 2007, 53(2): 610–621

38. Siegel N P, Ellis M W, Nelson D J, et al. Single domain PEMFC model based on agglomerate catalyst geometry. Journal of Power Sources, 2003, 115(1): 81–89

39. Zhang J, Cao P, Xu L, et al. Modeling nanostructured catalyst layer in PEMFC and catalyst utilization. Frontiers of Chemical Science and Engineering in China, 2011, 5(3): 297–302

40. Wu R, Liao Q, Zhu X, et al. Pore network modeling of cathode catalyst layer of proton exchange membrane fuel cell. International Journal of Hydrogen Energy, 2012, 37(15): 11255–11267

41. Khan M A, Sundén B, Yuan J. Analysis of multi-phase transport phenomena with catalyst reactions in polymer electrolyte membrane fuel cells: a review. Journal of Power Sources, 2011, 196(19): 7899–7916

42. Nguyen P T, Berning T, Djilali N. Computational model of a PEM fuel cell with serpentine gas flow channels. Journal of Power Sources, 2004, 130(1–2): 149–157

43. Tjaden B, Brett D J L, Shearing P R. Tortuosity in electrochemical devices: a review of calculation approaches. International Materials Reviews, 2018, 63(2): 47–67

44. Wei L, Liao Z H, Suo Z, et al. Numerical study of cold start performance of proton exchange membrane fuel cell with coolant

circulation. International Journal of Hydrogen Energy, 2019, 44(39): 22160–22172

45. Wei L, Dafalla A M, Jiang F M. Effects of reactants/coolant non-uniform inflow on the cold start performance of PEMFC stack. International Journal of Hydrogen Energy, 2020, 45(24): 13469–13482

46. Chippar P, Ju H. Evaluating cold-start behaviors of end and intermediate cells in a polymer electrolyte fuel cell (PEFC) stack. Solid State Ionics, 2012, 225: 85–91

47. Meng H. Numerical analyses of non-isothermal self-start behaviors of PEM fuel cells from subfreezing startup temperatures. International Journal of Hydrogen Energy, 2008, 33(20): 5738–5747

48. Bradean R, Haas H, Desousa A, et al. Models for predicting MEA water content during fuel cell operation and after shutdown. In: 2005 AIChE Annual Meeting and Fall Showcase. Cincinnati, OH, US, 2005, 10983–10990

49. Tajiri K, Tabuchi Y, Wang C Y. Isothermal cold start of polymer electrolyte fuel cells. Journal of the Electrochemical Society, 2007, 154(2): B147–B152

50. Dafalla A M, Wei L, Liao Z H, et al. Effects of clamping pressure on cold start behavior of polymer electrolyte fuel cells. Fuel Cells (Weinheim), 2019, 19(3): 221–230

51. Macauley N, Lujan R W, Spernjak D, et al. Durability of polymer electrolyte membrane fuel cells operated at subfreezing temperatures. Journal of the Electrochemical Society, 2016, 163(13): F1317–F1329